Check for updates

A single-molecule graphene quantum dot: a novel efficient photosensitizer for photodynamic cancer therapy†

Jintao Chen, [ID] Shiru Yin, Futing Yang, Shengnan Guo, [ID] Jiaojiao Zhang, Zhenming Lu and Tian Gao [ID] *

Graphene quantum dots (GQDs) can efficiently generate reactive oxygen species (ROS) under light irradiation, demonstrating significant potential for photodynamic therapy (PDT) applications. However, GQDs are often multicomponent mixtures with highly complex structures, which significantly hinders their clinical applications. Therefore, it is urgent to design and synthesize well-defined GQDs with excellent PDT performance. In this work, a novel single-molecule hydrophilic pure graphene quantum dot (HPGQD), containing 132 sp^2 conjugated carbon atoms, was prepared through an organic synthetic route using single-benzene-ring molecules as precursors. The HPGQD features a unique D-12A structure, comprising one large electron donor center and 12 electron acceptors, which grants it exceptional ROS release capabilities with a singlet oxygen ($^1O_2$) quantum yield of 0.85. Notably, under light irradiation, the HPGQD can rapidly generate abundant ROS within 30 s and scavenge them after 10 min, which holds promise for eliminating the need for prolonged light avoidance in patients undergoing PDT. It has been successfully applied to both *in vitro* (IC$_{50}$: 0.22 μmol L^{-1}) and *in vivo* (tumor weight inhibition rate: 71%) PDT for cancer treatment. The innovative design, synthesis, and PDT application of the single-molecule HPGQD pave the way towards accelerated clinical applications of carbon nanomaterials, advancing the frontier of nanotherapeutic research.

Introduction

Graphene quantum dots (GQDs), as emerging zero-dimensional (0-D) carbon nanomaterials, show great potential in biomedical applications, especially in cancer therapy.[1–4] However, the typical synthesis of GQDs always results in extremely complex and uncontrollable structures, which significantly hinders their clinical applications.[5,6] The traditional synthesis methods of GQDs can be categorized into two major approaches: top-down or bottom-up.[7,8] However, both methods often rely on drastic reactions such as hydrothermal/solvothermal reactions and intense oxidation reactions, making it challenging to prepare GQDs with well-defined structure.[9–11] Notably, a precise structure is crucial for the safety and efficacy evaluation of therapeutic agents, thereby being necessary for medicinal applications.[12–17] Consequently, it is urgent to develop an

innovative method to prepare GQDs with accurate and controllable molecular structure.[18–22]

Photodynamic therapy (PDT) is a promising, non-invasive approach in cancer treatment, exhibiting universal applicability and significant potential for clinical applications.[23–25] Within the framework of PDT, photosensitizers (PSs) play a pivotal role in the generation of reactive oxygen species (ROS) under light irradiation.[26,27] Nevertheless, both organic and nanoscale PSs exhibit certain deficiencies that hinder their utility.[28–31] Firstly, the efficiency of ROS release by current PSs remains insufficient, necessitating multiple treatments within a single course, which increased the treatment burden on patients. Secondly, a significant drawback associated with commonly used PSs is the prolonged period of photo-blocking required post-PDT. Patients are often compelled to remain in darkness for extended durations, even up to half a year, leading to considerable physical and mental discomfort. This constraint significantly impacts the quality of life of patients undergoing PDT. Thirdly, the underlying mechanism of PDT for nano-photosensitizers (nano-PSs) remains controversial, posing challenges in the rational design of their structures and the optimization of their performance.[32] This lack of clarity hinders the progress in developing advanced nano-PSs with predictable and enhanced therapeutic outcomes.[33] Thus, in the face of these challenges, it is urgent to develop a comprehensive strategy that

Interdisciplinary Institute of NMR and Molecular Sciences, Key Laboratory of Hubei Province for Coal Conversion and New Carbon Materials, School of Chemistry and Chemical Engineering, Institute of Advanced Materials and Nanotechnology, Wuhan University of Science and Technology, Wuhan 430081, China. E-mail: gaotian@whu.edu.cn

† Electronic supplementary information (ESI) available. See DOI: https://doi.org/10.1039/d5sc03226a

facilitates the syntheses of highly efficient nano-PSs with customizable structures.[5,34,35] Ideally, these nano-PSs should eliminate the need for prolonged photo-blocking, thereby enhancing patient comfort and adherence to treatment protocols.[36]

Inspiringly, a single-molecule hydrophilic pure graphene quantum dot (HPGQD) with a unique structure was synthesized using an innovative organic approach. Notably, the HPGQD possesses a novel "D-12A" structure, comprising a large electron donor and twelve electron acceptors, exhibiting exceptional capabilities in releasing ROS. Within a brief duration of 30 s, the HPGQD efficiently generates a significant amount of ROS, and effectively scavenges ROS after continuous irradiation for 10 min. Consequently, during PDT utilizing the HPGQD, prolonged light avoidance by patients is unnecessary. The underlying mechanism of this phenomenon has been elucidated at the molecular level. Furthermore, the HPGQD has been successfully applied *in vitro* (IC$_{50}$: 0.22 µmol L^{-1}) and *in vivo* (tumor weight inhibition rate: 71%) for cancer PDT. This work paves a new way to the design and synthesis of pure single-molecule GQDs as promising PSs for both efficient and safe PDT. Consequently, it will significantly enhance the biomedical application of carbon nanomaterials, thereby paving the way for more effective and patient-friendly cancer treatment options.

Results and discussion

Design and organic synthesis of the single-molecule "D-12A" type HPGQD

GQDs with intact structures are highly prone to aggregation and precipitation due to π–π stacking, posing significant challenges for their dispersion in solutions.[37,38] To overcome this issue, organic synthesis was employed to prepare Pure GQD (PGQD) with methoxycarbonyl groups on the surface and HPGQD with carboxylate salts from molecules with the benzene ring. PGQD and HPGQD, each containing a core of 132 sp^2 – conjugated carbon atoms, were successfully designed and synthesized (Fig. 1a). In detail, to achieve precise control over the structure of HPGQD, a synthetic pathway originating from a simple benzene ring was designed. Initially, compound 2 was synthesized using 3-bromoacetophenone[39,40] (Fig. S1, S4–S7†), and compound 5 was synthesized using 4-bromo-phenylacetic acid[41] (Fig. S2, S8–S13†). As shown in Fig. 1a, compounds 2 and 5 underwent a Diels–Alder reaction, resulting in the formation of
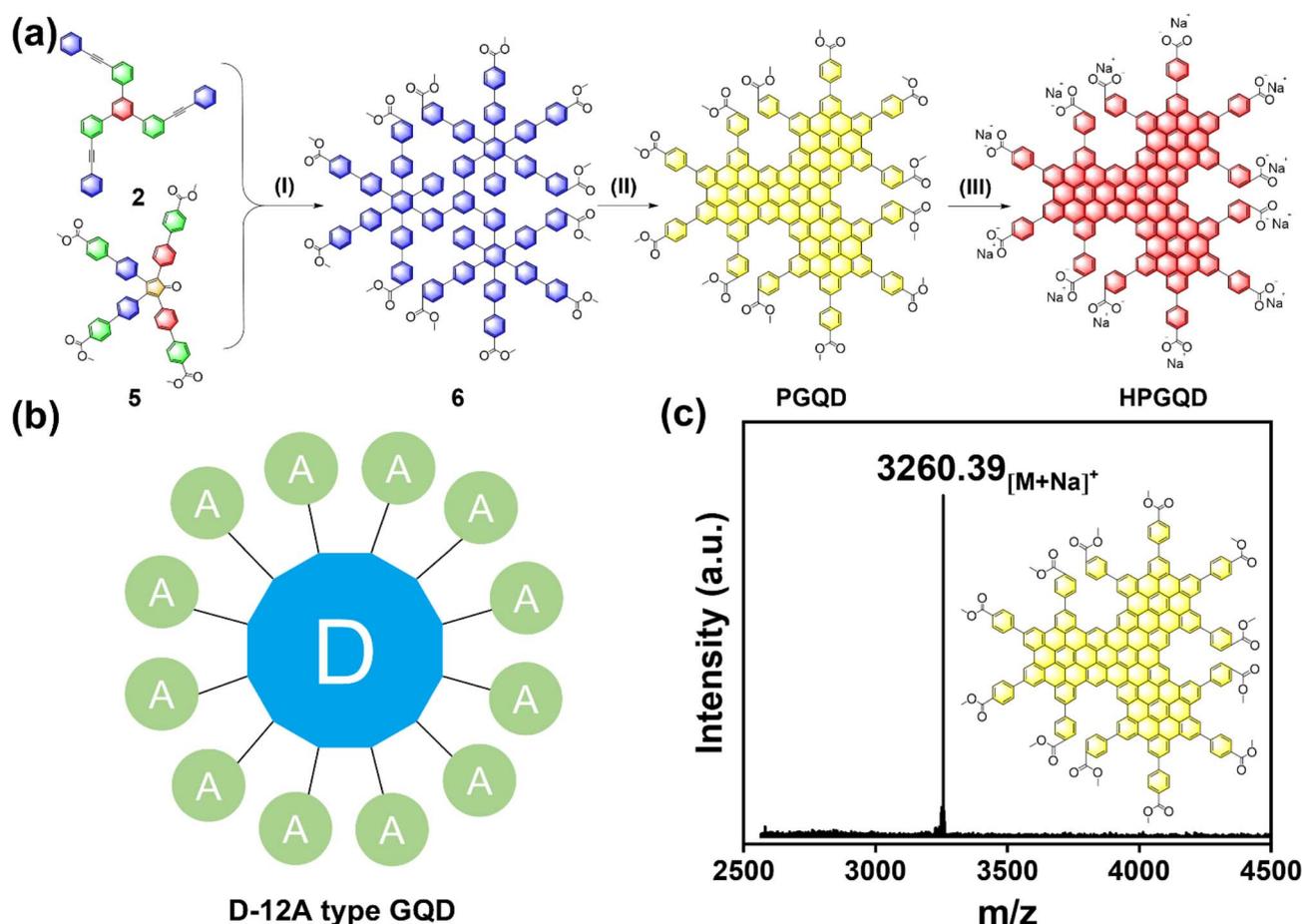

Fig. 1 Design and organic synthesis of single-molecule "D-12A" type HPGQD. (a) Synthetic route of HPGQD. (I) Ph$_2$O, 250 °C, 10 h, yield: 34%. (II) FeCl$_3$, CH$_3$NO$_2$, DCM, rt, 2 h, yield: 34%. (III) NaOH, THF/MeOH/H$_2$O = 1/1/2, v/v/v, 60 °C, 24 h, yield: 91%. (b) Schematic diagram of single-molecule "D-12A" type HPGQD. D: electron donor; A: electron acceptor. D-12A: one electron donor-12 electron acceptors. (c) MALDI-TOF-MS spectrum of PGQD bound to an Na$^+$ ion (matrix: TCNQ).

polycyclic aromatic hydrocarbons (PAH) (compound 6) (Fig. S3, S14 and S15†). Following this reaction, PGQD was synthesized by dehydrogenating the PAH *via* a Scholl reaction, with ferric chloride serving as the catalyst. Ultimately, HPGQD, containing functional carboxylate groups at the edges, was obtained through a hydrolysis reaction.

The unique structure of HPGQD features one electron donor (the inner graphite core) and 12 electron acceptors (the edge functional carboxylate groups), as shown in Fig. 1b. Notably, MALDI-TOF-MS analysis revealed a molecular weight of 3260.39 Da for PGQD binding with an Na^+ ion, with no obvious impurity signals (Fig. 1c). Fig. S16–S21† display the detailed mass spectrum of all intermediates. Molecular weight information is crucial for nanomedicine.

The MALDI-TOF-MS analysis provided convincing and reliable validation of the composition and purity of the PGQD. It also confirms the successful synthesis of single-molecule HPGQD, which is synthesized from PGQD through a typical and efficient salt-forming reaction. Consequently, this work utilized organic synthesis to prepare pure inorganic GQD, thereby bridging the gap between organic and inorganic chemistry and enabling atomic-level controllable synthesis of nanomaterials.
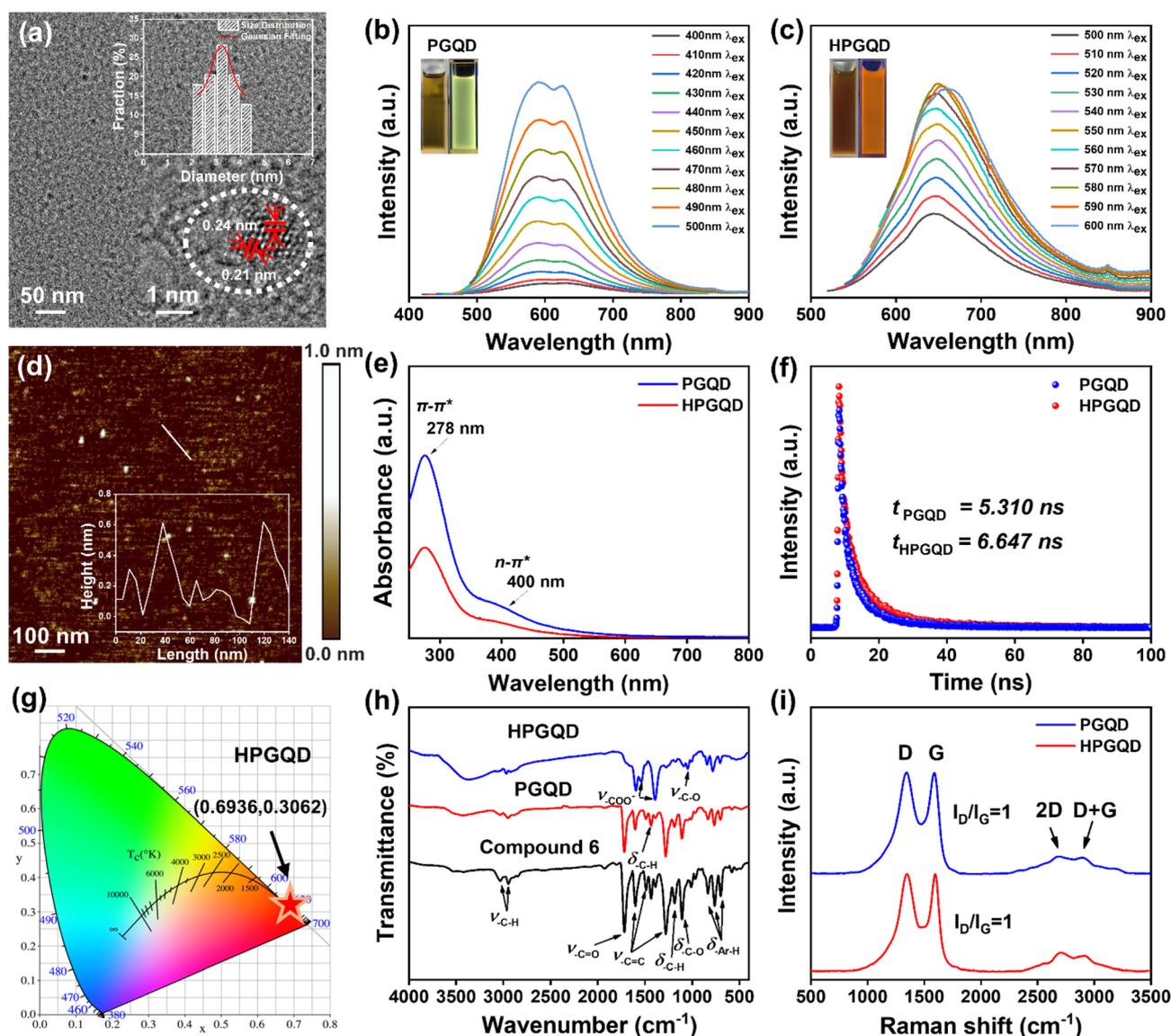

Fig. 2 The morphology, surface structure and optical properties of PGQD and HPGQD. (a) HRTEM image of HPGQD (top-right inset shows statistical size distribution and Gaussian curve fitting, bottom-right inset shows lattice fringes). (b) PL emission spectrum of PGQD (in DCM, 7.5 µmol L^{-1}). Insets display pictures of PGQD under natural light (left) and 365 nm UV light (right). (c) PL emission spectrum of HPGQD (in H_2O, 7.5 µmol L^{-1}). Insets display pictures of HPGQD under natural light (left) and 365 nm UV light (right). (d) AFM image of HPGQD (bottom right inset shows the height profile along the marked line in the AFM image). (e) UV-vis spectra of PGQD (in DCM, 7.5 µmol L^{-1}) and HPGQD (in H_2O, 7.5 µmol L^{-1}). (f) PL decay curves of PGQD and HPGQD. (g) The CIE color coordinates of HPGQD. (h) FTIR spectra of PAH (compound 6), PGQD and HPGQD. (i) Raman spectra of PGQD and HPGQD.

Morphology, surface structure and optical properties

Transmission electron microscopy (TEM) images reveal that the HPGQD exhibits a particle size of 3.2 ± 0.1 nm, with a narrow size distribution, as depicted in Fig. 2a. Notably, the two-dimensional lattice fringes of HPGQD are distinctly observable, revealing lattice spacings of 0.21 nm and 0.24 nm, corresponding to the typical graphite (100) and (200) crystal planes, respectively, as depicted in the inset of Fig. 2a and S22b.† This observation suggests the presence of a complete graphite core structure within HPGQD. The particle size distribution of HPGQD in the TEM picture aligns closely with Gaussian fitting, consistent with results obtained from molecular structure calculations (Fig. S22a†). Over a seven-day period, the hydrodynamic size of HPGQD, as measured daily by dynamic light scattering (DLS), remained essentially unchanged in phosphate buffered saline (PBS) supplemented with human serum albumin (HSA). This observation, illustrated in Fig. S23a,† underscores the excellent stability of HPGQD. The DLS spectrum of HPGQD on the seventh day is displayed in Fig. S23b,† showing an average hydrodynamic diameter of 10.8 ± 0.2 nm with a narrow particle size distribution. The zeta potential of −23 ± 1 mV confirms the stable mono-dispersion of HPGQD in PBS solution (Table S1†). Furthermore, atomic force microscopy (AFM) was employed to measure the thickness of HPGQD (Fig. 2d). The height profile extracted from the AFM scan (Fig. 2d, inset) revealed a thickness of less than 0.6 nm, consistent with a monolayer graphene structure for HPGQD.

The optical properties of GQDs were investigated using a fluorescence spectrophotometer (FL). The FL spectra revealed that both PGQD and HPGQD exhibited excitation-independent characteristics, as evidence by their unchanged photoluminescence (PL) emission peaks regardless of excitation wavelength (Fig. 2b and c). The property of non-excitation-dependent emission stems from molecular-state emission, which corroborates that the prepared GQD possesses a well-defined single fluorescent molecule structure. As shown in Fig. 2b, PGQD displayed two distinct emission centers at 590 nm and 625 nm, emitting yellow fluorescence. In contrast, HPGQD exhibited a prominent emission peak at 650 nm (Fig. 2c), resulting in red fluorescence, with a broad absorption spectrum in the 400–600 nm range in the excitation spectrum (Fig. S24a†). The HPGQD PL emission spectrum featured a single peak located near the absorption band in the low-energy region, indicating that its PL emission originates from absorption in this region.[42] These PL properties further confirm the structural integrity of HPGQD, including the graphitic core and edge states. In addition, the UV-vis spectra of PGQD and HPGQD revealed absorption bands at 278 and 400 nm (Fig. 2e and S24b†). The strong absorption peak at 278 nm is attributed to the π–π* transition of C=C bonds within the nanographene core, while weaker absorption at 400 nm is due to the combined effect of the n–π* transitions of C=C/C=O bonds and π–π* charge transfer transitions at the edges of HPGQD.[43] Meanwhile, compound 6 exhibits a narrow absorption peak in its UV-vis spectra at 285 nm (Fig. S24d†). In contrast, both PGQD and HPGQD display broad absorption peaks in their UV-vis spectra

with a concentration-dependent nature, indicating successful macrocyclic ring closure, the formation of a fully sp² conjugated structure, and the consistency of their core structures (Fig. S24e andf†). Furthermore, the band gap of HPGQD was determined to be 3.80 eV using the Tauc plot method, which aligns with the observed band gap reduction associated with a PL redshift (Fig. S24c†).[44]

Additionally, PL decay curves were fitted using a double-exponential decay function, resulting in average lifetimes of 5.310 ns for PGQD and 6.647 ns for HPGQD, respectively (Fig. 2f and Table S2†).[45] Notably, the average lifetime of HPGQD was slightly prolonged compared to PGQD, which is attributed to the enhanced charge carrier capture facilitated by the adjacent 12 methoxycarbonyl groups. Furthermore, the PL quantum yields (PLQY) for PGQD and HPGQD were measured to be 2.82% and 3.23%, respectively (Fig. S25a and b†). In comparison with PGQD, HPGQD demonstrates a marginal increase in PLQY. This enhancement is ascribed to the surface activation induced by the saltification of methoxycarbonyl groups, effectively suppressing the process of radiative recombination. The CIE color coordinates for HPGQD were determined to be (0.6936, 0.3062), indicating a pure red color emission (Fig. 2g). Consequently, HPGQD exhibits potential applications in bioimaging.

Furthermore, the fluorescence stability of HPGQD in PBS was investigated in the temperature range of 0–50 °C (Fig. S26a†). Under 520 nm excitation, HPGQD exhibits a stable emission peak at 650 nm in PBS across all tested temperatures (0–50 °C), confirming its robust structural integrity and resistance to thermal interference in physiological environments. The fluorescence intensity at 650 nm demonstrates a linear increase with rising temperature ($R^2 = 0.997$; Fig. S26b†). This behavior aligns with thermally activated electron transition processes in carbon-based quantum dots, further supporting the excellent photostability of HPGQD.

The FTIR spectra of PAH (compound 6), PGQD, and HPGQD exhibited consistent characteristic peaks, revealing stretching vibrations of C–H bonds at 3029 and 2946 cm⁻¹, C=O bonds at 1718 cm⁻¹, COO⁻ groups at 1542 and 1398 cm⁻¹, and C=C bonds at 1602, 1491, and 1280 cm⁻¹. Notably, the bending vibrations of C–H bonds in the fingerprint region of the benzene ring for PGQD and HPGQD, specifically at 833, 762, and 698 cm⁻¹, were weakened compared to those of PAH (compound 6), indicating the formation of an sp² carbon-conjugated region. Furthermore, a decrease in peak intensities within the 700–840 cm⁻¹ region, which represents C–H vibrations, was observed during the transformation from PAH (compound 6) to single-molecule GQD, suggesting successful PAH cyclization in the liquid phase. Residual peaks within this range correspond to collective bending of C–H bonds located at the outer and inner edges of the molecule (Fig. 2h and Table S3†).[46]

The Raman spectra of PGQD and HPGQD, excited at a wavelength of 532 nm (Fig. 2i), exhibit two distinct and characteristic peaks: the D peak located at 1350 cm⁻¹ and the G peak at 1590 cm⁻¹. These peaks are indicative of graphitic materials, thereby confirming the graphitic nature of PGQD and HPGQD. Typically, conventional graphene-based materials

(such as graphene, graphene oxide, carbon nanotubes, and carbon quantum dots) display high I_D/I_G ratios, reflecting the presence of numerous edge defects.[47] In contrast, PGQD and HPGQD feature armchair-type edge configurations, which introduce edge-defective structures akin to those in conventional carbon materials.[48] The high I_D values observed for PGQD and HPGQD are attributed to their small particle size and abundant edges. Notably, the Raman spectra indicate I_D/I_G ratios of 1 for both PGQD and HPGQD, confirming their fully sp^2 conjugated core structures and consistent edge configurations. Additionally, broader 2D band combination peaks are observed within the range of 2500–3200 cm^{-1}, including the 2D peak at 2720 cm^{-1} and the D + G peak at 2900 cm^{-1}. These bands align with previously reported Raman spectra of bottom-up synthesized nanographene, suggesting an organically controlled synthesis approach for achieving higher-quality nanographene.[46]

X-ray diffraction (XRD) analysis (Fig. S27†) reveals that HPGQD exhibits characteristic long-range ordered features, with diffraction peaks attributable to reflections from the (002), (110), (004), (200), and (112) crystallographic planes. The emergence of these peaks indicates that HPGQD possesses a highly crystalline in-plane structure. The corresponding interplanar spacings were calculated using the Bragg equation ($n\lambda = 2d\sin\theta$) and are summarized in Table S4.† In contrast to conventional graphene, which displays only a broadened (002) peak (associated with disordered interlayer stacking), HPGQD demonstrates pronounced high-angle diffraction peaks, signifying its exceptional in-plane crystallinity. The ultra-small size of HPGQD (<10 nm) amplifies quantum confinement effects, which enhances localized in-plane lattice ordering while weakening interlayer interactions. This suppresses the (002) peak and intensifies diffraction signals from in-plane facets (*e.g.*, (110), (100), (200)). Furthermore, oxygen-containing functional groups (–COO$^-$) introduced during synthesis are anchored at the edge sites of HPGQD. These functional groups affect the hexagonal symmetry of the lattice, thereby activating higher-order diffraction peaks (*e.g.*, (112)) that are typically weak or absent in the pristine graphene system.

Based on the characterization data from multiple dimensions, it is demonstrated that the as-synthesized HPGQD is a novel single-molecule GQD. First, molecular mass uniformity is demonstrated by MALDI-TOF-MS (Fig. 1c), where a singular peak at $m/z = 3260.39$ exclusively corresponds to the theoretical mass of the HPGQD molecule, with no precursor residues detected. Additionally, the purity of all synthetic intermediates is rigorously verified by NMR and MS (Fig. S5–S21†), eliminating the interference of nano-molecules on the purity of HPGQD. Second, monodisperse particles with a uniform diameter of 3.2 ± 0.1 nm and a characteristic height of 0.6 nm are observed by TEM and AFM (Fig. 2a and d), consistent with single-layer molecular dimensions. Third, the formation of an sp^2-conjugated framework is evidenced by FTIR spectroscopy (Fig. 2h), wherein attenuation of benzene C–H bending vibrations (833–698 cm^{-1}) is accompanied by residual edge modes that preclude small-molecule contamination. Fourth, Raman spectroscopy (Fig. 2i) reveals diagnostic D/G bands ($I_D/I_G = 1$) and 2D peaks

(2720 cm^{-1}), confirming a graphitic core with armchair edges intrinsic to finite-sized GQDs. Finally, the XRD data indicate that HPGQD exhibits a high degree of crystallinity, with narrow and distinct signal peaks, suggesting that HPGQD possesses a novel nanoscale molecular structure. Thus, characterizations including molecular weight determination (MS), NMR, morphology analyses (TEM, AFM), spectroscopic techniques (FTIR, Raman), and XRD collectively demonstrate that HPGQD is a single-layer single-molecule GQD with nanoscale dimensions, an intact carbon sp^2-conjugated core, and a well-defined molecular structure.

Excellent ROS release ability

The "D-12A" type single-molecule HPGQD enriches the electron transport path and enhances electron transport efficiency, thereby promoting exciton generation and boosting the ROS generation capacity. Subsequently, an evaluation of the ROS generation ability of HPGQD was conducted.

As shown in Fig. 3a, under light irradiation, the PL signal of the HPGQD + DCFH + L solution exhibited a significant increase, indicating the generation of abundant ROS. Further investigations revealed the impact of concentration, irradiation time, and irradiation wavelength on ROS generation (Fig. S28a–d†). The optimal parameters for maximizing ROS release efficacy were identified as follows: a concentration of 7.5 μmol L^{-1}, an irradiation wavelength of 460 nm, and an irradiation duration of 30 s (Fig. S28d†). Notably, HPGQD demonstrates exceptional ROS generation ability, releasing abundant ROS within 30 s of exposure to excitation light. However, the ROS was scavenged gradually after 10 min. Notably, even at the micromolar level, HPGQD also demonstrates the capacity to instantaneously generate substantial amounts of ROS, offering promising prospects for future *in vivo* PDT for cancer. To verify the type of ROS produced by HPGQD, electron spin resonance (ESR) spectroscopy was employed. Under irradiation from a xenon lamp (300 W) for 30 s, TEMP and DMPO were utilized as trapping agents for $^1O_2$ and $O_2^{\cdot-}$ (or $\cdot$OH), respectively. Upon irradiation, a characteristic $^1O_2$-induced TEMPO signal was observed, with no other ROS signals detected (Fig. 3b and c). Absolute quantitative data, presented in Table S5,† further confirmed the excellent singlet oxygen ($^1O_2$) generation capability of HPGQD.

Additionally, under following irradiation (white light, 20 mW cm^{-2}), the absorbance of DPBF at 415 nm decreased progressively with increasing irradiation time, ultimately being completely consumed within 30 s. This demonstrates that DPBF specifically reacts with $^1O_2$ generated by HPGQD, forming an endoperoxide and decomposing to 1,2-dibenzoylbenzene (Fig. 3e and S29a†). In addition, no blue agent was formed for indicator Methylene Blue (MB) when HPGQD was irradiated, demonstrating that no $\cdot$OH was produced (Fig. 3f and S29b†). Consequently, it is concluded that the ROS type generated by HPGQD is $^1O_2$ (Fig. 3g).

The $^1O_2$ quantum yield of HPGQD, calculated using eqn (S7) (ESI),† is 0.85, which is significantly superior to traditional organic photosensitizers and offers notable advantages in PDT
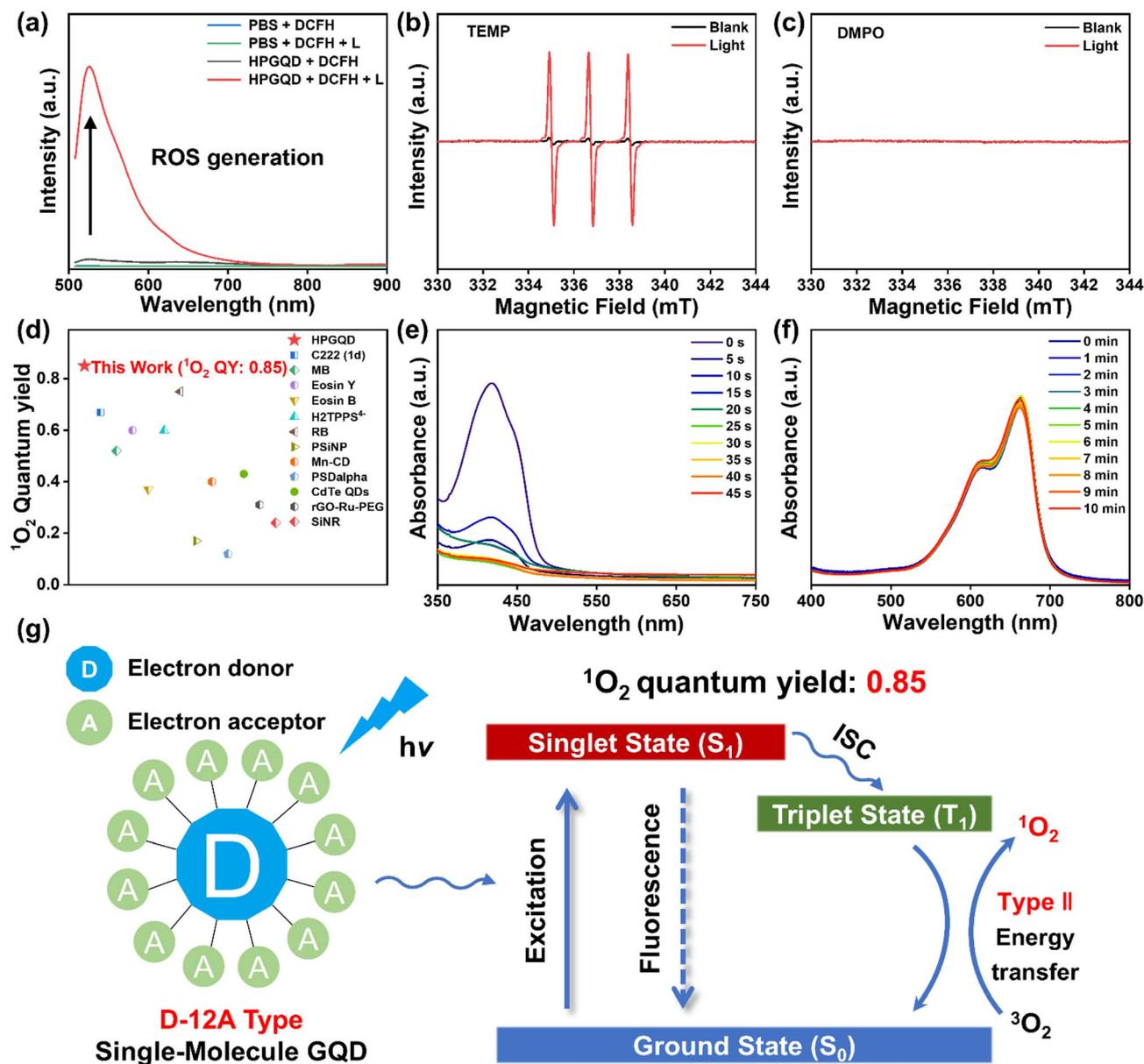
Fig. 3 Excellent ROS generation ability of HPGQD. (a) ROS generation test. DCFH (1×10^{-7} mol L^{-1}) was used to detect ROS generation of HPGQD with/without light irradiation (460 nm, 20 mW cm^{-2}, 30 s). (b) ESR-based ROS species test utilizing TEMP as an indicator probe for singlet oxygen ($^1O_2$). The ESR signal indicative of $^1O_2$ was obtained after exposing HPGQD solution to a xenon lamp (300 W) for 30 s, with TEMP serving as the trapping agent. (c) ESR-based ROS species test utilizing DMPO as an indicator probe for $^\bullet$OH. The ESR signal indicative of $^\bullet$OH was obtained after exposing HPGQD solution to a xenon lamp (300 W) for 30 s, with DMPO serving as the trapping agent. (d) Comparative analysis of $^1O_2$ quantum yield of previous works. (e) UV-vis-based ROS species and generation efficiency test using DPBF as a probe for $^1O_2$. HPGQD (0.83 μmol L^{-1}, 3 mL) was irradiated at different times and $^1O_2$ was detected using DPBF (0.25 mg mL^{-1}, 200 μL). (f) UV-vis-based ROS species and generation efficiency test using MB as a probe for $^\bullet$OH. HPGQD (0.83 μmol L^{-1}, 3 mL) was irradiated at different times and $^\bullet$OH was detected using MB (300 μmol L^{-1}, 1 mL). (g) Mechanism of generating $^1O_2$ by HPGQD.

applications. In comparison to previous studies on $^1O_2$-producing materials and commercial photosensitizers, the $^1O_2$ quantum yield of HPGQD has a significant advantage, highlighting its immense potential in cancer PDT (Fig. 3d and Table S6†). Under white light irradiation at 20 mW cm^{-2}, the absorbance of Na$_2$-ADPA solution at 378 nm gradually decreased with increasing irradiation time, indicating the degradation of Na$_2$-ADPA by $^1O_2$ generated from HPGQD and Rose bengal (RB) (Fig. S30†). Additionally, DPBF was employed to evaluate the

type II ROS generating capacity of HPGQD, Chlorin e6 (Ce6), and RB. Compared with the typical type II photosensitizers Ce6 and RB, HPGQD completely consumed DPBF within 150 s, showing stronger type II ROS generation ability (Fig. S31 and S32†).

Based on the precise molecular structure, the mechanism of ROS release by GQD under light irradiation was thoroughly explored and revealed. Fig. S33† exhibits the combined use of FL and ESR methods to verify the type of ROS generated by

HPGQD. With the increase of irradiation time, HPGQD interacts with $^1O_2$ to form HPGQD-EP, and then forms the C–O–O–C group in HPGQD-EP. This process disrupts the sp^2 conjugated in the core structure and destroys the electron-donating framework. Therefore, the capacity for ROS release through energy transfer is interrupted, leading to a decrease in $^1O_2$ levels (Fig. S34†). Similarly, compound 6, as a PAH molecule without a planar carbon sp^2 conjugation structure, does not generate ROS under irradiation, confirming that the core conjugated structure of HPGQD is the vital electron donor (Fig. S35a†). The formation of HPGQD-EP in turn alters the core-plane carbon sp^2 coupling structure of HPGQD, resulting in reduced fluorescence output (Fig. S35b and c†). The "D-12A" type structure of HPGQD is essential for rapid $^1O_2$ generation within 30 s, and the conjugated structure transformation can completely eliminate $^1O_2$ within 10 min of subsequent irradiation. Therefore, after HPGQD injection and brief irradiation, patients do not require prolonged light avoidance, mitigating significant physical and psychological discomfort. HPGQD holds great promise as next-generation nano-PSs.

In vitro cellular PDT efficacy

Furthermore, in vitro cellular PDT efficacy was evaluated. The 4T1 cells were utilized to evaluate toxicity in the absence of light and PDT effect upon irradiation with HPGQD.

Under dark conditions, 4T1 cells maintained high viability when co-incubated with various concentrations of HPGQD for 72 h, even up to 60 μmol L^{-1}, indicating excellent biocompatibility and minimal cellular toxicity of HPGQD in darkness (Fig. S36†). Conversely, under 460 nm laser irradiation, the cellular viability of 4T1 cells co-incubated with HPGQD decreased significantly, demonstrating a concentration- and irradiation time-dependent effect (Fig. 4a). To exclude the influence of irradiation alone, 4T1 cells were irradiated with a 460 nm laser (1.5 W cm^{-2}, 72 h) with varied irradiation times and powers, exhibiting a survival rate as high as 90%, indicating that the ROS was generated by HPGQD which is responsible for cell death (Fig. S37†). IC_{50} values under different irradiation durations were determined through dose–response curve fitting (Fig. S38†). Specifically, under 10 min irradiation, the IC_{50} of HPGQD was only 0.22 μmol L^{-1} (Table S7†). From a patient perspective, HPGQD exhibits therapeutic efficacy at lower concentrations and shorter irradiation durations. Notably, HPGQD possesses a unique self-protection property, enabling it to scavenge ROS after 10 min of irradiation, thereby ceasing ROS generation even under subsequent light exposure, including sunlight. Following HPGQD injection and a brief phototherapy session, the need for prolonged light avoidance is eliminated, substantially mitigating the physical and psychological burden on patients. Compared with carbon-based nanomaterials previously reported for PDT, HPGQD shows great advantages in terms of drug concentration and irradiation time, positioning it as a promising candidate for the next generation of novel nano-PSs (Fig. 4b and Table S8†).

Confocal laser scanning microscopy (CLSM) showed a notable time-dependent uptake of HPGQD by cells (Fig. 4c). The results showed that the fluorescence intensity of HPGQD progressively
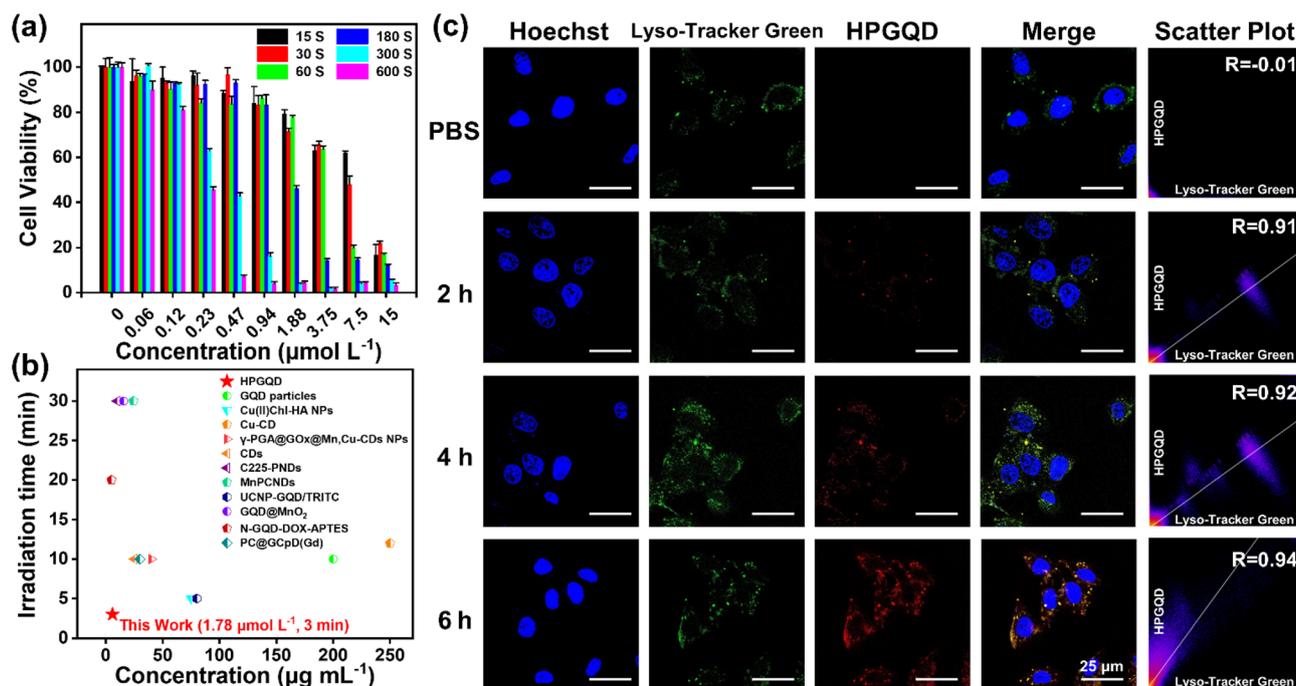

Fig. 4 In vitro cellular PDT efficacy of HPGQD. (a) Cytotoxicity assay of HPGQD under light irradiation. In vitro cellular toxicity assessment of 4T1 cells following co-incubation with HPGQD (460 nm, 20 mW cm^{-2}, irradiation for 15 s, 30 s, 60 s, 180 s, 300 s, and 600 s). (b) Comparative analysis IC_{50} values of different carbon-based nanomaterials in PDT, considering drug concentration and irradiation time. (c) CLSM images of HPGQD co-localisation with lysosomes. CLSM images of 4T1 cells co-incubated with HPGQD (3 μmol L^{-1}) for 2, 4, and 6 h. Scatter plots of pixel distributions of red vs. green channels (scale bar: 25 μm).

increased with extended culture duration. Notably, after 6 h of incubation, the distribution of HPGQD in the cells significantly overlapped with the lysosomes, suggesting lysosomal-mediated internalization. Confocal imaging analysis using Lyso-Tracker Green revealed a high fluorescence overlap between HPGQD and lysosomes, with a Pearson's correlation coefficient more than 0.9, confirming its predominant lysosomal enrichment. Thus, it underscores the promising potential of HPGQD as a lysosome-targeted nanomedicine. Furthermore, CLSM showed a significant positive correlation between cellular uptake of HPGQD and ROS production. Specifically, cells ingesting HPGQD exhibited substantial ROS generation (Fig. 5a). And then, the colocalization coefficient between HPGQD and the DCFH-DA dye was quantitatively analyzed. The fluorescence overlap (Pearson's correlation coefficient) exhibited a significantly positive temporal correlation, confirming that enhanced cellular uptake of HPGQD directly correlates with increased ROS generation. This progressive ROS accumulation, monitored over time, underscores the dose-dependent oxidative stress response induced by HPGQD internalization. It is worth noting that the ROS releasing position is wider than that of the HPGQD taken up, indicating that the generated ROS spread in the cells to enhance the therapeutic effect. Flow cytometry (FCM) analysis confirmed the absence of ROS in cells under dark conditions. As the co-incubation time increased, the accumulation of HPGQD within cells intensified, leading to an elevated production of ROS upon light exposure.

Both CLSM and FCM results consistently confirmed that HPGQD exhibits an excellent PDT effect *in vitro* in cells (Fig. 5b, c and S39†).

Compared to NIR-absorbing materials, HPGQD exhibits a relatively short UV-absorbing wavelength, posing a constraint for deep tumor PDT. Nevertheless, HPGQD stands out as a novel nano-PS characterized by its remarkable capacity for generating $^1O_2$, rendering it efficacious *in vitro* for cellular PDT. Consequently, investigating the *in vivo* PDT efficacy of HPGQD is imperative for this nascent material, serving as a crucial step towards its clinical application. The optical properties of the single-molecule GQD can be enhanced by incorporating upconversion materials, constructing a Förster resonance energy transfer (FRET) structure, and optimizing the edge conformation or functional groups. These enhancements will boost the absorption in the NIR region, thereby promoting tissue penetration ability for effective deep-tissue therapy.

In vivo PDT efficacy

HPGQD exhibits great potential for integrated application in the diagnosis and treatment of cancer. To investigate its PDT and bioimaging effects *in vivo*, HPGQD was injected into nude mice. As shown in Fig. 6a, *in vivo* fluorescence imaging revealed that HPGQD emits bright red light in the tumor region, indicating the excellent bioimaging capability and tumor aggregation effect of HPGQD. Fig. 6b further illustrates that HPGQD accumulated in the tumor for a duration of up to 72 h, confirming
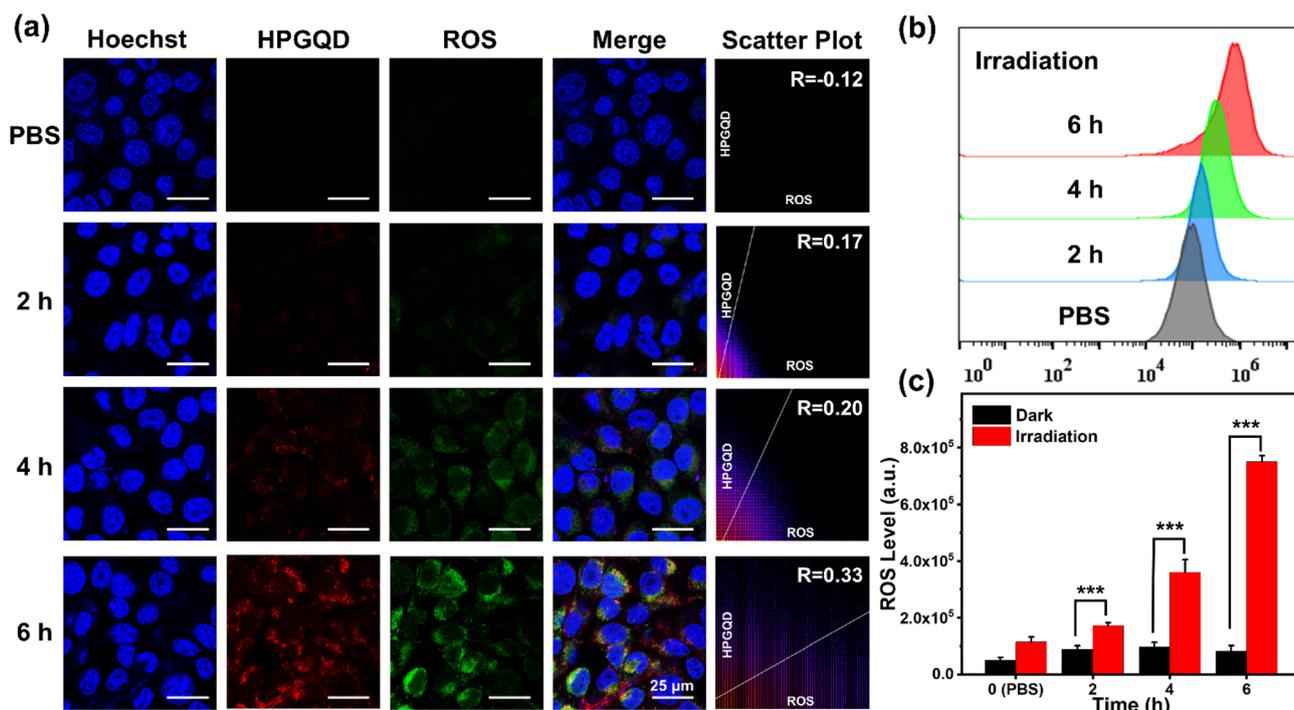

Fig. 5 *In vitro* cellular ROS generation of HPGQD. (a) CLSM images of ROS generation by HPGQD. ROS generation of 4T1 cells co-incubated with HPGQD (3 μmol L^{-1}) for 2, 4 and 6 h and irradiated (460 nm, 20 mW cm^{-2}, 30 s). Scatter plots of pixel distributions of red *vs.* green channels (scale bar: 25 μm). (b) FCM detection of ROS level generation by HPGQD with irradiation. ROS generation of 4T1 cells co-incubated with HPGQD (3 μmol L^{-1}) for 2, 4 and 6 h and irradiated (460 nm, 20 mW cm^{-2}, 30 s) used by DCFH-DA. (c) ROS levels of 4T1 cells co-incubated with HPGQD (3 μmol L^{-1}) for 2, 4 and 6 h (with/without irradiation). All data are presented as means ± SD ($n = 3$). *p*-values were calculated by a Two-tailed test using GraphPad Prism software, ***, $p < 0.001$.
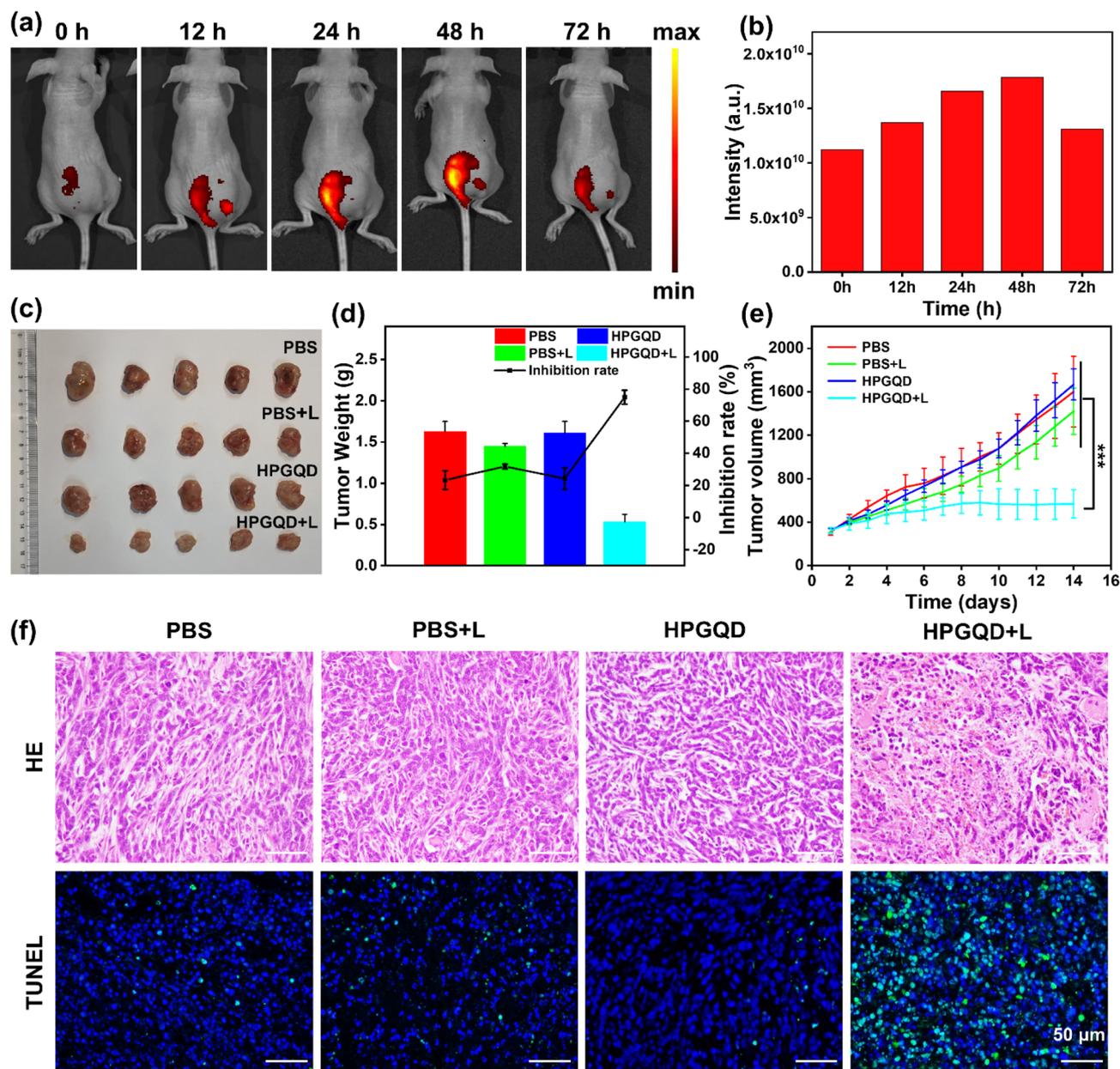
Fig. 6 *In vivo* PDT efficacy of HPGQD. (a) *In vivo* FL images of mice. The *in vivo* FL images of the 4T1-tumor-bearing model at different times after injection of HPGQD (100 μL, 150 μmol L^{-1}). (b) Quantitative analysis of *in vivo* FL images after injection of HPGQD. (c) Photograph of the tumour after dissection. The photograph of 4T1 tumors removed from mice on the 14th day after PDT treatment. (d) Quantitative analysis of tumor weights on the 14th day after PDT treatment. Data are presented as mean ± SD ($n = 5$). (e) The changes in volume of subcutaneous tumors treated for 14 days. Data are presented as mean ± SD ($n = 5$). (f) H&E and TUNEL staining images of different groups. (scale bar: 50 μm). *p*-values were calculated by one-way ANOVA using GraphPad Prism software, ***, $p < 0.001$.

that HPGQD possesses the cancer cell targeting ability. A comparative analysis of the images revealed that the FL intensity of HPGQD in cells peaked at 48 h. Subsequently, a standard PDT protocol for cancer treatment was established, involving the injection of HPGQD every 3 d and irradiated every 2 d. Over a 14-day treatment period, pre-dissection photographs presented in Fig. S40a† showed a significant inhibition of tumor growth in mice undergoing PDT. Photographs of 4T1 tumors removed from mice on the 14th day post-PDT treatment are shown in Fig. 6c. In the PBS, PBS + L (light irradiation), and

HPGQD groups, tumor sizes of the mice continued to proliferate rapidly. However, mice receiving HPGQD + L treatment exhibited a remarkable decrease in tumor weight, achieving tumor growth inhibition rates of 71% and 63% based on weight and volume, respectively (Fig. 6d and S40c†). As shown in Fig. 6e, the volume changes of subcutaneous tumors in the mice exhibited a similar pattern to the change in tumor weight, both clearly evidencing the remarkable PDT efficacy of HPGQD.

Simultaneously, the biosafety of HPGQD was demonstrated to be superior in this study. The effects of HPGQD-mediated

PDT on mice were comprehensively investigated through weight monitoring, histological analysis, and blood routine analysis. These methodologies were employed to explore the reliability and safety of this novel nanomedicine. Body weight, which serves as a crucial indicator for evaluating treatment-related side effects, demonstrated minimal fluctuations across all treated mice, as shown in Fig. S40b,† suggesting the absence of obvious adverse effects attributable to HPGQD.

Subsequent pathological analysis of excised tumor tissues was conducted using H&E and TUNEL staining to assess their histological features. Cells in the HPGQD + L group exhibited shrinkage, nuclear rupture, high tumor elimination rates, and a significant degree of tumor cell apoptosis. This indicates that effective tumor elimination occurred through cell apoptosis, which was a result of ROS generation induced by HPGQD-mediated PDT. Conversely, cells in the other groups maintained intact morphologies with no notable alterations (Fig. 6f).

Furthermore, an *ex vivo* analysis utilizing H&E staining was conducted on critical organs, encompassing the heart, liver, spleen, lungs, and kidneys (Fig. S41†). This analysis revealed the preservation of distinct cytoplasmic and nuclear features in all groups, thus attesting to the absence of any apparent organ damage. In addition, blood analysis revealed that the white blood cell, red blood cell, and platelet counts of the mice remained within the normal physiological range, thereby indicating the absence of significant biotoxicity associated with HPGQD (Fig. S42 and Table S9†). Collectively, the above results unequivocally demonstrate that PDT treatment with HPGQD exerts no notable impact on the body weight, tissue cells, or blood system of mice, thus affirming its superior biosafety. As a single-molecule nanomaterial exhibiting remarkable biocompatibility and potent antitumor effects through PDT, HPGQD possesses immense potential for application in PDT for cancer, making it a promising candidate for future clinical implementation.

Conclusions

This work achieved a breakthrough in the development of GQD, with the successfully synthesis of HPGQD featuring a specific monomolecular formula ($Na_{12}C_{216}H_{78}O_{24}$) through organic synthetic methods. HPGQD, due to its unique and innovative D-12A structure, exhibited superior ROS-releasing capabilities, rapidly generating abundant ROS within 30 s and effectively scavenging them after prolonged irradiation beyond 10 min. Consequently, patients treated with HPGQD do not need to stay in a light-avoiding environment for extended periods, thereby overcoming a significant clinical challenge associated with PDT. Furthermore, HPGQD exhibits exceptional PDT performance for cancer, with an IC_{50} value of 0.22 µmol L^{-1} *in vitro* (4T1 cell lines) and a tumor weight inhibition rate of 71% *in vivo* (nude mice). In addition, red light-emitting HPGQD has been successfully employed for both *in vitro* and *in vivo* bioimaging applications. HPGQD demonstrates significant potential for theranostic applications, serving as a dual-purpose approach for cancer diagnosis and treatment, thereby efficiently propelling the advancements of nanomedicine.

The successful preparation of single-molecule GQD not only bridges the gap between organic and inorganic chemistry but also establishes an excellent paradigm for molecular synthesis of diverse nanomaterials. The design of the D-12A type HPGQD photosensitizer leverages the properties of nanomaterials and mechanisms of organic photosensitizers, effectively expanding the structural diversity of photosensitizers and significantly advancing the application of nanomaterials in PDT. The breakthrough in single-molecule synthesis technology effectively enhances the consistency, safety, and optimizability of nanomedicines, facilitating improvements in their safety and efficacy and thereby greatly promoting their transition into practical clinical applications.

Data availability

The general information, methods, NMR spectra, MS spectra, synthetic details, biological details, and supplementary discussions associated with this article are provided in the ESI.†

Author contributions

T. G. conducted conceptual design and overall division of labor. J. C. and T. G. conceived and designed the study. J. C., S.·Y., S. G. and J. Z. synthesized and characterized the molecules. J. C., S. Y. and F. Y. performed the cell and animal studies. J. C. and T. G. analyzed the data and drew the Figures. J. C. and T. G. performed visualization drawing. S. G., J. Z. and F. Y. helped in the experiments. J. C. and T. G. drafted the manuscript. Z. L. and T. G. revised the manuscript. J. C. and T. G. contributed to the writing of this paper. T. G. conducted the review and editing.

Conflicts of interest

The authors declare no competing financial interest.

Acknowledgements

Notes and references

1 H. J. Liu, Z. M. Deng, Z. H. Zhang, W. C. Lin, M. Q. Zhang and H. Wang, Graphene quantum dots as metal-free nanozymes for chemodynamic therapy of cancer, *Matter*, 2024, 7, 1–14.
2 Y. Yang, B. Wang, X. Zhang, H. Li, S. Yue, Y. Zhang, Y. Yang, M. Liu, C. Ye, P. Huang and X. Zhou, Activatable Graphene

Quantum-Dot-Based Nanotransformers for Long-Period Tumor Imaging and Repeated Photodynamic Therapy, *Adv. Mater.*, 2023, **35**, 2211337.

3 Y. Zhang, G. Kim, Y. Zhu, C. Wang, R. Zhu, X. Lu, H.-C. Chang and Y. Wang, Chiral Graphene Quantum Dots Enhanced Drug Loading into Small Extracellular Vesicles, *ACS Nano*, 2023, **17**, 10191–10205.

4 B. Lee, K. Gries, A. R. Valimukhametova, R. L. McKinney, R. Gonzalez-Rodriguez, U. C. Topkiran, J. Coffer, G. R. Akkaraju and A. V. Naumov, In Vitro Prostate Cancer Treatment *via* CRISPR-Cas9 Gene Editing Facilitated by Polyethyleneimine-Derived Graphene Quantum Dots, *Adv. Funct. Mater.*, 2023, **33**, 2305506.

5 X. Zhang, L. Li, B. Wang, Z. Cai, B. Zhang, F. Chen, G. Xing, K. Li and S. Qu, Donor-Acceptor Type Supra-Carbon-Dots with Long Lifetime Photogenerated Radicals Boosting Tumor Photodynamic Therapy, *Angew. Chem., Int. Ed.*, 2024, **63**, e202410522.

6 D. Kim, J. M. Yoo, H. Hwang, J. Lee, S. H. Lee, S. P. Yun, M. J. Park, M. Lee, S. Choi, S. H. Kwon, S. Lee, S. H. Kwon, S. Kim, Y. J. Park, M. Kinoshita, Y. H. Lee, S. Shin, S. R. Paik, S. J. Lee, S. Lee, B. H. Hong and H. S. Ko, Graphene quantum dots prevent alpha-synucleinopathy in Parkinson's disease, *Nat. Nanotechnol.*, 2018, **13**, 812–818.

7 L. L. Shi, B. Y. Wang and S. Y. Lu, Efficient bottom-up synthesis of graphene quantum dots at an atomically precise level, *Matter*, 2023, **6**, 728–760.

8 Y. Yan, J. Gong, J. Chen, Z. Zeng, W. Huang, K. Pu, J. Liu and P. Chen, Recent Advances on Graphene Quantum Dots: From Chemistry and Physics to Applications, *Adv. Mater.*, 2019, **31**, e1808283.

9 H. Zhang, H. Guo, D. Li, Y. Zhang, S. Zhang, W. Kang, C. Liu, W. Le, L. Wang, D. Li and B. Dai, Halogen doped graphene quantum dots modulate TDP-43 phase separation and aggregation in the nucleus, *Nat. Commun.*, 2024, **15**, 2980.

10 M. J. Sweetman, S. M. Hickey, D. A. Brooks, J. D. Hayball and S. E. Plush, A Practical Guide to Prepare and Synthetically Modify Graphene Quantum Dots, *Adv. Funct. Mater.*, 2019, **29**, 1808740.

11 Z. Gu, S. Zhu, L. Yan, F. Zhao and Y. Zhao, Graphene-Based Smart Platforms for Combined Cancer Therapy, *Adv. Mater.*, 2019, **31**, e1800662.

12 Y. Y. Ju, X. X. Shi, S. Y. Xu, X. H. Ma, R. J. Wei, H. Hou, C. C. Chu, D. Sun, G. Liu and Y. Z. Tan, Atomically Precise Water-Soluble Graphene Quantum Dot for Cancer Sonodynamic Therapy, *Adv. Sci.*, 2022, **9**, e2105034.

13 G. Li, Z. Liu, W. Gao and B. Tang, Recent advancement in graphene quantum dots based fluorescent sensor: Design, construction and bio-medical applications, *Coord. Chem. Rev.*, 2023, **478**, 214966.

14 X.-H. Ma, X. Gao, J.-Y. Chen, M. Cao, Q. Dai, Z.-K. Jia, Y.-B. Zhou, X.-J. Zhao, C. Chu, G. Liu and Y.-Z. Tan, Soluble Nanographene C222: Synthesis and Applications for Synergistic Photodynamic/Photothermal Therapy, *J. Am. Chem. Soc.*, 2024, **146**, 2411–2418.

15 H. Zhao, Y. Wang, Q. Chen, Y. Liu, Y. Gao, K. Müllen, S. Li and A. Narita, A Nanographene-Porphyrin Hybrid for Near-Infrared-Ii Phototheranostics, *Adv. Sci.*, 2024, **11**, e2309131.

16 X. Zhu, Q. Chen, H. Zhao, Q. Yang, Goudappagouda, M. Gelléri, S. Ritz, D. Ng, K. Koynov, S. H. Parekh, V. K. Chetty, B. K. Thakur, C. Cremer, K. Landfester, K. Müllen, M. Terenzio, M. Bonn, A. Narita and X. Liu, Intrinsic Burst-Blinking Nanographenes for Super-Resolution Bioimaging, *J. Am. Chem. Soc.*, 2024, **146**, 5195–5203.

17 Z.-H. Wu, X. Zhu, Q. Yang, Y. Zagranyarski, K. Mishra, H. Strickfaden, R. P. Wong, T. Basché, K. Koynov, M. Bonn, C. Li, X. Liu and K. Müllen, Near-Infrared Perylenecarboximide Fluorophores for Live-Cell Super-Resolution Imaging, *J. Am. Chem. Soc.*, 2024, **146**, 7135–7139.

18 R. Liu, D. Wu, X. Feng and K. Müllen, Bottom-up fabrication of photoluminescent graphene quantum dots with uniform morphology, *J. Am. Chem. Soc.*, 2011, **133**, 15221–15223.

19 A. Narita, X. Y. Wang, X. Feng and K. Müllen, New advances in nanographene chemistry, *Chem. Soc. Rev.*, 2015, **44**, 6616–6643.

20 P. Ruffieux, S. Wang, B. Yang, C. Sanchez-Sanchez, J. Liu, T. Dienel, L. Talirz, P. Shinde, C. A. Pignedoli, D. Passerone, T. Dumslaff, X. Feng, K. Müllen and R. Fasel, On-surface synthesis of graphene nanoribbons with zigzag edge topology, *Nature*, 2016, **531**, 489–492.

21 S. Zhao, J. Lavie, L. Rondin, L. Orcin-Chaix, C. Diederichs, P. Roussignol, Y. Chassagneux, C. Voisin, K. Müllen, A. Narita, S. Campidelli and J.-S. Lauret, Single photon emission from graphene quantum dots at room temperature, *Nat. Commun.*, 2018, **9**, 3470.

22 Z. Zhang, H. Zhu, J. Gu, H. Shi, T. Hirose, L. Jiang, Y. Zhu, D. Zhong and J. Wang, Nonplanar Nanographene with a Large Conjugated π-Surface, *J. Am. Chem. Soc.*, 2024, **146**, 24681–24688.

23 D. W. Felsher, Cancer revoked: oncogenes as therapeutic targets, *Nat. Rev. Cancer*, 2003, **3**, 375–379.

24 P. Agostinis, K. Berg, K. A. Cengel, T. H. Foster, A. W. Girotti, S. O. Gollnick, S. M. Hahn, M. R. Hamblin, A. Juzeniene, D. Kessel, M. Korbelik, J. Moan, P. Mroz, D. Nowis, J. Piette, B. C. Wilson and J. Golab, Photodynamic therapy of cancer: An update, *Ca-Cancer J. Clin.*, 2011, **61**, 250–281.

25 U. Chilakamarthi and L. Giribabu, Photodynamic Therapy: Past, Present and Future, *Chem. Rec.*, 2017, **17**, 775–802.

26 J. Ge, M. Lan, B. Zhou, W. Liu, L. Guo, H. Wang, Q. Jia, G. Niu, X. Huang, H. Zhou, X. Meng, P. Wang, C.-S. Lee, W. Zhang and X. Han, A graphene quantum dot photodynamic therapy agent with high singlet oxygen generation, *Nat. Commun.*, 2014, **5**, 4596.

27 S. S. Lucky, K. C. Soo and Y. Zhang, Nanoparticles in Photodynamic Therapy, *Chem. Rev.*, 2015, **115**, 1990–2042.

28 J. Karges, Clinical Development of Metal Complexes as Photosensitizers for Photodynamic Therapy of Cancer, *Angew. Chem., Int. Ed.*, 2021, **61**, e202112236.

29 V.-N. Nguyen, Z. Zhao, B. Z. Tang and J. Yoon, Organic photosensitizers for antimicrobial phototherapy, *Chem. Soc. Rev.*, 2022, **51**, 3324–3340.

30 B. Nasseri, E. Alizadeh, F. Bani, S. Davaran, A. Akbarzadeh, N. Rabiee, A. Bahadori, M. Ziaei, M. Bagherzadeh, M. R. Saeb, M. Mozafari and M. R. Hamblin, Nanomaterials for photothermal and photodynamic cancer therapy, *Appl. Phys. Rev.*, 2022, **9**, 011317.

31 Y. Zhang, B.-T. Doan and G. Gasser, Metal-Based Photosensitizers as Inducers of Regulated Cell Death Mechanisms, *Chem. Rev.*, 2023, **123**, 10135–10155.

32 M. Tavakkoli Yaraki, B. Liu and Y. N. Tan, Emerging Strategies in Enhancing Singlet Oxygen Generation of Nano-Photosensitizers Toward Advanced Phototherapy, *Nano-Micro Lett.*, 2022, **14**, 123.

33 T. C. Pham, V.-N. Nguyen, Y. Choi, S. Lee and J. Yoon, Recent Strategies to Develop Innovative Photosensitizers for Enhanced Photodynamic Therapy, *Chem. Rev.*, 2021, **121**, 13454–13619.

34 C. Zhao, C. Qu, Y. Hu, F. Wu, S. Liu, F. Cai, Y. Chen, Y. Qiu and Z. Shen, Orbicular-Donor-Acceptor System in N-doped Nanographene for Highly Efficient NIR-II Photothermal Therapy, *Adv. Healthcare Mater.*, 2024, **13**, 2402545.

35 Y. Jiang, S. Huang, H. Ma, J. Weng, X. Du, Z. Lin, J. Kim, W. You, H. Zhang, D. Wang, J. S. Kim and H. Sun, RNA-Activatable Near-Infrared Photosensitizer for Cancer Therapy, *J. Am. Chem. Soc.*, 2024, **146**, 25270–25281.

36 M. Kolarikova, B. Hosikova, H. Dilenko, K. Barton-Tomankova, L. Valkova, R. Bajgar, L. Malina and H. Kolarova, Photodynamic therapy: Innovative approaches for antibacterial and anticancer treatments, *Med. Res. Rev.*, 2023, **43**, 717–774.

37 X. Yan, B. S. Li and L. S. Li, Colloidal Graphene Quantum Dots with Well-Defined Structures, *Acc. Chem. Res.*, 2013, **46**, 2254–2262.

38 D. Medina-Lopez, T. Liu, S. Osella, H. Levy-Falk, N. Rolland, C. Elias, G. Huber, P. Ticku, L. Rondin, B. Jousselme, D. Beljonne, J.-S. Lauret and S. Campidelli, Interplay of structure and photophysics of individualized rod-shaped graphene quantum dots with up to 132 sp^2 carbon atoms, *Nat. Commun.*, 2023, **14**, 4728.

39 V. S. Iyer, M. Wehmeier, J. D. Brand, M. A. Keegstra and K. Müllen, From Hexa-peri-hexabenzocoronene to "Superacenes", *Angew. Chem., Int. Ed.*, 1997, **36**, 1604–1607.

40 H. Hu, A. Zhang, L. Ding, X. Lei and L. Zhang, Simple and Convenient Synthesis of 1,3,5-triarylbenzenes from Ketones, *J. Chem. Res.*, 2019, **2007**, 720–721.

41 L. Han, Y. W. Zhang, W. P. Chen, X. Cheng, K. Q. Ye, J. Y. Zhang and Y. Wang, Assembly of twisted luminescent architectures based on acenaphtho[1,2-k]fluoranthene derivatives, *Chem. Commun.*, 2015, **51**, 4477–4480.

42 J. Zhao, J. Xu, H. Huang, K. Wang, D. Wu, R. Jasti and J. Xia, Appending Coronene Diimide with Carbon Nanohoops Allows for Rapid Intersystem Crossing in Neat Film, *Angew. Chem., Int. Ed.*, 2024, **63**, e202400941.

43 C. Xia, J. Zhong, X. Han, S. Zhu, Y. Li, H. Liu and B. Yang, The Formation Mechanism of Carbonized Polymer Dots: Crosslinking-Induced Nucleation and Carbonization, *Angew. Chem., Int. Ed.*, 2024, **63**, e202410519.

44 H. Wang, X. C. Liu, X. Y. Yan, J. W. Fan, D. W. Li, J. S. Ren and X. G. Qu, A MXene-derived redox homeostasis regulator perturbs the Nrf2 antioxidant program for reinforced sonodynamic therapy, *Chem. Sci.*, 2022, **13**, 6704–6714.

45 M. Park, Y. Jeong, H. S. Kim, W. Lee, S. H. Nam, S. Lee, H. Yoon, J. Kim, S. Yoo and S. Jeon, Quenching-Resistant Solid-State Photoluminescence of Graphene Quantum Dots: Reduction of π–π Stacking by Surface Functionalization with POSS, PEG, and HDA, *Adv. Funct. Mater.*, 2021, **31**, 2102741.

46 M. Sarker, C. Dobner, P. Zahl, C. Fiankor, J. Zhang, A. Saxena, N. Aluru, A. Enders and A. Sinitskii, Porous Nanographenes, Graphene Nanoribbons, and Nanoporous Graphene Selectively Synthesized from the Same Molecular Precursor, *J. Am. Chem. Soc.*, 2024, **146**, 14453–14467.

47 Z. Li, L. Deng, I. A. Kinloch and R. J. Young, Raman spectroscopy of carbon materials and their composites: Graphene, nanotubes and fibres, *Prog. Mater. Sci.*, 2023, **135**, 101089.

48 J.-B. Wu, M.-L. Lin, X. Cong, H.-N. Liu and P.-H. Tan, Raman spectroscopy of graphene-based materials and its applications in related devices, *Chem. Soc. Rev.*, 2018, **47**, 1822–1873.